Journal of Atmospheric and Solar-Terrestrial Physics 73 (2011) 1254–1269

Contents lists available at ScienceDirect

Journal of Atmospheric and Solar-Terrestrial Physics

journal homepage: www.elsevier.com/locate/jastp

Multiple, distant (40°) in situ observations of a magnetic cloud and a corotating interaction region complex

C.J. Farrugia [a,*], D.B. Berdichevsky [b], C. Möstl [c], A.B. Galvin [a], M. Leitner [d], M.A. Popecki [a], K.D.C. Simunac [a], A. Opitz [e], B. Lavraud [e], K.W. Ogilvie [f], A.M. Veronig [g], M. Temmer [c], J.G. Luhmann [h], J.A. Sauvaud [e]

[a] Space Science Center, University of New Hampshire, Durham, NH, USA
[b] Maryland, USA
[c] Space Research Institute, Austrian Academy of Sciences, Graz, Austria
[d] Institute of Astro- and Particle Physics, University of Innsbruck, Innsbruck, Austria
[e] CESR, Toulouse, France
[f] NASA/Goddard Space Flight Center, Greenbelt, MD, USA
[g] Institute of Physics, University of Graz, Graz, Austria
[h] Space Sciences Laboratory, University of Berkeley, Berkeley, USA

ARTICLE INFO

Article history:
Received 31 March 2010
Received in revised form
31 August 2010
Accepted 3 September 2010
Available online 18 September 2010

Keywords:
MC–CIR interaction
Double flux rope
Shock analysis

ABSTRACT

We report a comprehensive analysis of in situ observations made by Wind and the STEREO probes (STA, STB) of a complex interaction between a magnetic cloud (MC) and a corotating interaction region (CIR) occurring near the heliospheric current sheet (HCS) on November 19–21, 2007. The probes were separated by 0.7 AU ($\sim 40^{\circ}$) with a spread in heliographic latitudes (4.8,° 2.2,° and -0.4,° for STB, Wind and STA, respectively). We employ data from the MFI, SWE and 3DP instruments on Wind, and the PLASTIC and IMPACT suites on STEREO. STB, located east of Earth, observed a forward shock followed by signatures of a MC. The MC took the role of the HCS in that the polarity of the interplanetary magnetic field (IMF) on exit was the reverse of that on entry. A passage through a plasma sheet was observed. Along the Sun–Earth line Wind observed a stream interface (SI) between a forward and a reverse shock. A MC, compressed by the CIR, was entrained in this. STA, located 20° to the west of Earth, saw a MC which was not preceded by a shock. A SI trailed the transient. The shocks are examined using various methods and from this it is concluded that the forward shock at Wind—but not at STB—was driven by the MC. Examining the MC by Grad–Shafranov reconstruction, we find evidence of a double-flux rope structure at Wind and STA and possibly also at STB. The orientations are at variance with the notion of a large-scale flux tube being observed at the three spacecraft. We find consistency of this with the directional properties of the solar wind "strahl" electrons. We examine aspects of the geomagnetic response and find a double-dip storm corresponding to the two interplanetary triggers. The minimum Dst phase was prolonged and the geoeffects were intensified due to the interaction. We conclude that while the formation of compound streams is a common feature of interplanetary space, understanding their components when CIRs are involved is a complicated matter needing numerical simulations and/or more in situ observations for its complete elucidation.

1. Introduction

The launch of STEREO in October 2006 occurred just before the start of a long and extreme solar activity minimum phase which lasted three years. During this time very few coronal mass ejections (CMEs) were observed at the Sun; the energy densities of the solar wind, both magnetic as well as kinetic, decreased due to lower-than-average magnetic fields and low average velocities; and geomagnetic activity was at an unprecedented low, the last major storm (Dst ≤ -100 nT, not including the effect of magnetopause currents) having occurred in October 2006. The interplanetary medium itself was populated by a long succession of slow and fast streams. Many stream interaction regions (SIRs) were observed. SIRs occur when fast streams overtake slow streams, causing a compression region of enhanced pressure and magnetic field strength. SIRs that recur over solar rotations are called corotating interaction regions (CIRs; Jian et al., 2006).

Compound streams is the name given by Burlaga et al. (1987) to two or more simple streams which interact in space. Typical cases are interactions of (i) a magnetic cloud/interplanetary coronal mass ejection (MC/ICME) with another MC/ICME transient; and (ii) a transient with a SIR or CIR. Further downstream

* Corresponding author.
E-mail address: charlie.farrugia@unh.edu (C.J. Farrugia).

1364-6826/$ - see front matter © 2010 Elsevier Ltd. All rights reserved.
doi:10.1016/j.jastp.2010.09.011

from 1 AU, or even sometimes at 1 AU, they may form global merged interaction regions (GMIRs; Burlaga, 1995; Burlaga et al., 2003; Rouillard et al., 2010c). The case of a CIR interacting with a MC was studied by Burlaga et al. (1987) using three spacecraft separated by tens of degrees in longitude. Compound streams are associated with intensified geomagnetic activity (Burlaga et al., 1987; Dal Lago et al., 2002), and a complex response in cosmic ray modulation (Burlaga et al., 1985). For these various reasons compound streams are of considerable scientific interest.

Two recent significant discoveries were made, which were possible in part due to the imaging capability of the SECCHI instrument suite (Howard et al., 2008) on the two STEREO spacecraft (STEREO-AHEAD [STA] and STEREO-BEHIND [STB]) when they were distant from each other. One concerned the propagation of CMEs in interplanetary space. First visible in coronagraphs, their passage through the inner heliosphere could be tracked by the Heliospheric Imager, using the scattering of sunlight by electrons (Thomson scattering; Vourlidas and Howard, 2006), and later observed in situ as they passed over another spacecraft (Davis et al., 2009, Möstl et al., 2009b,c). Features near the Sun could thus be related with those at 1 AU, a procedure that has obvious implications for space weather forecasting.

The second concerned the slow solar wind itself. Unlike the fast wind from coronal holes, the origins of the slow wind are subject to debate and two or three possible origins are discussed, none mutually exclusive. During solar minimum, the streamer belt, in which is embedded the heliospheric current sheet (HCS), is quite well aligned with the solar heliographic equator. At high latitudes are the coronal holes, sources of the fast wind. The magnetic field structure at the feet of the streamers contains open field lines bracketing closed loops and arcades above which the streamer forms and the slow wind escapes. Work by Sheeley (1997, 1999) and Wang et al. (2000) had shown evidence for blobs of plasma advancing anti-sunward from the streamer belts. This work was continued with STEREO, where techniques were developed (J-maps, Sheeley et al., 1999, 2008; Rouillard et al., 2008, 2009) to track the density enhancements in CIRs. Surprisingly, it was found that CIRs often exhibit transient brightenings. It was shown that in these cases the CIRs can entrain ICMEs and MCs (Rouillard et al., 2009, 2010a,b). In the same spirit, but using a different methodology, Kilpua et al. (2009) recently documented the presence of many small transients lying typically in the slow solar wind. They were generally being passively convected with the wind with no radial expansion and they lacked many of the signatures usually associated with ICMEs. Almost invariably, there was no evidence on the Sun of the expulsion of CMEs associated with them. These developments, favored by the multi-point observational capability and the long solar minimum 2007–2009, have opened new vistas in our understanding of the slow solar wind.

This paper is a further contribution to such studies. It concerns a MC, which is most likely of a double-rope structure, observed by STB, WIND/ACE and STA, when STA and STB were separated by $\sim 40^\circ$ in heliographic inertial longitude. At the same time a CIR was overtaking the MC. The different corotation and radial delays lead to different effects of the CIR on the transient at the distant spacecraft. We first describe the data at each spacecraft, trying to distinguish transient from corotating features. We obtain the orientation of the MC by minimum variance analysis and force-free fitting, i.e. by methods which have inherent assumptions on the geometry and which also presume the absence of external forces. Since the latter is not likely to hold in this case, we can thus obtain an idea of the distortions caused by these forces. We then examine the MC by the method of Grad–Shafranov (GS) reconstruction, applicable to configurations in hydrostatic equilibrium and containing a direction of translational invariance (i.e. an axis). We link the results of this with inferences drawn from the directional properties of the solar wind strahl (e.g. Ogilvie et al., 1971; Pilipp et al., 1987), i.e., the high energy (>100 eV) electron component which is closely field-aligned and carries the heat flux away from the Sun. Further insight into this interaction is provided by an analysis of the shocks seen at the spacecraft. Finally, we take a look at major geomagnetic disturbances elicited by this complex and also try to estimate the effect of the interaction by subtracting the geoeffects of a pristine CIR seen one solar rotation earlier. In the final section we summarize our main findings.

2. Observations

2.1. Instruments

We report in situ data from STEREO and Wind. STA and STB carry the same complement of instruments. We employ plasma data from the PLASTIC instrument (Galvin et al., 2008), magnetic field data from MAG (Acuña et al., 2008), and electron data from SWEA (Sauvaud et al., 2008). MAG and SWEA form part of the IMPACT suite of instruments (Luhmann et al., 2008). All data are at 1 min resolution. Wind proton, electron and alpha particle observations are from the Solar Wind Experiment (SWE; Ogilvie and et al., 1995) and the 3-Dimensional Plasma Analyzer (3DP; Lin and et al., 1995). SWE key parameter data are at ~ 92 s time resolution, 3DP data at 3 s resolution, and electron data at 12 s resolution. Wind magnetic field data are from the Magnetic Field Investigation (MFI; Lepping and et al., 1995), where we use both the 3 s and the 60 s key parameter data.

2.2. STB

The locations of the three spacecraft, projected into the ecliptic plane, is given in Fig. 1. The Sun rotates from east to west (in an anticlockwise sense). At 12:00 UT, November 20, 2007, STB is at a heliocentric distance of 1.0381 AU with heliographic latitude and longitude $(4.77^\circ, -20.35^\circ)$. Corresponding data for STA are 0.9655 AU and $(-0.38,^\circ 20.23^\circ)$. Wind is in orbit around the Lagrangian L1 point upstream of Earth at a heliocentric distance is 0.99 AU and angular coordinates $(2.2,^\circ 0.0^\circ)$.

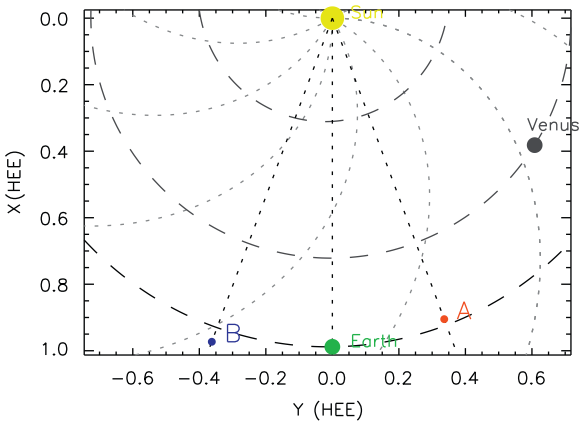

Fig. 1. The positions in the ecliptic plane of the STEREO spacecraft with respect to Earth on November 20, 2007. (HEE stands for heliocentric Earth ecliptic coordinates.) The heliospheric distances are 1.0381 AU and 0.9655 AU. The Wind spacecraft is orbiting the Lagrangian L1 point at a heliospheric distance of 0.99 AU. The heliographic latitudes are 4.77° (STB), 2.2° (Wind), and -0.38° (STA).

We next discuss the observations made by the various spacecraft, proceeding from east to west. Fig. 2 shows plasma and magnetic field measurements made by STB during the period 12:00 UT, November 19 to 24:00 UT, November 20. Displayed from top to bottom are the proton density (N; in red: alpha particle-to-proton number density ratio in percent with scale on the right), bulk speed (V), the east–west component of the velocity (VT) and temperature (T), the total field (B) and its components in the RTN coordinate system, the pressures (total [P_T] in black, magnetic [P_b] in red, and plasma [P_p] in blue), and the proton β (in red: the Alfvén Mach number with same scale as β). The RTN coordinates are defined such that the axis R points from the Sun to the spacecraft, axis T is perpendicular to it and points in the direction of planetary motion, and axis N points perpendicular to the RT plane such that the RTN system is right-handed. The red trace in panel 4 gives the expected proton temperatures after the statistical analysis of Lopez (1987).

The data show a gradual, stepwise transition from an initially slow (V $\sim 320\,\mathrm{km\,s^{-1}}$) to a fast ($\sim 620\,\mathrm{km\,s^{-1}}$) wind. Marked are various important features of this slow-to-fast solar wind transition. The first guideline from the left shows a fast forward shock (FS) where the density, speed, temperature and magnetic field strength undergo sharp increases. The period bracketed by the second and fourth guidelines (from $\sim 23:00$ UT, November 19 to 07:00 UT, November 20) shows a generally cold plasma of low proton beta with a strong magnetic field and a field vector which executes a large rotation. These properties define a MC (Burlaga et al., 1981). The last vertical guideline marks the arrival of a pressure wave. The gradients and the variation trends of some of the quantities indicate that it has not yet steepened into a (reverse) shock.

The high-density region starting at the third vertical guideline is likely to be a crossing of a high-beta plasma sheet. It does not satisfy the conditions for a stream interface (SI). By a SI we

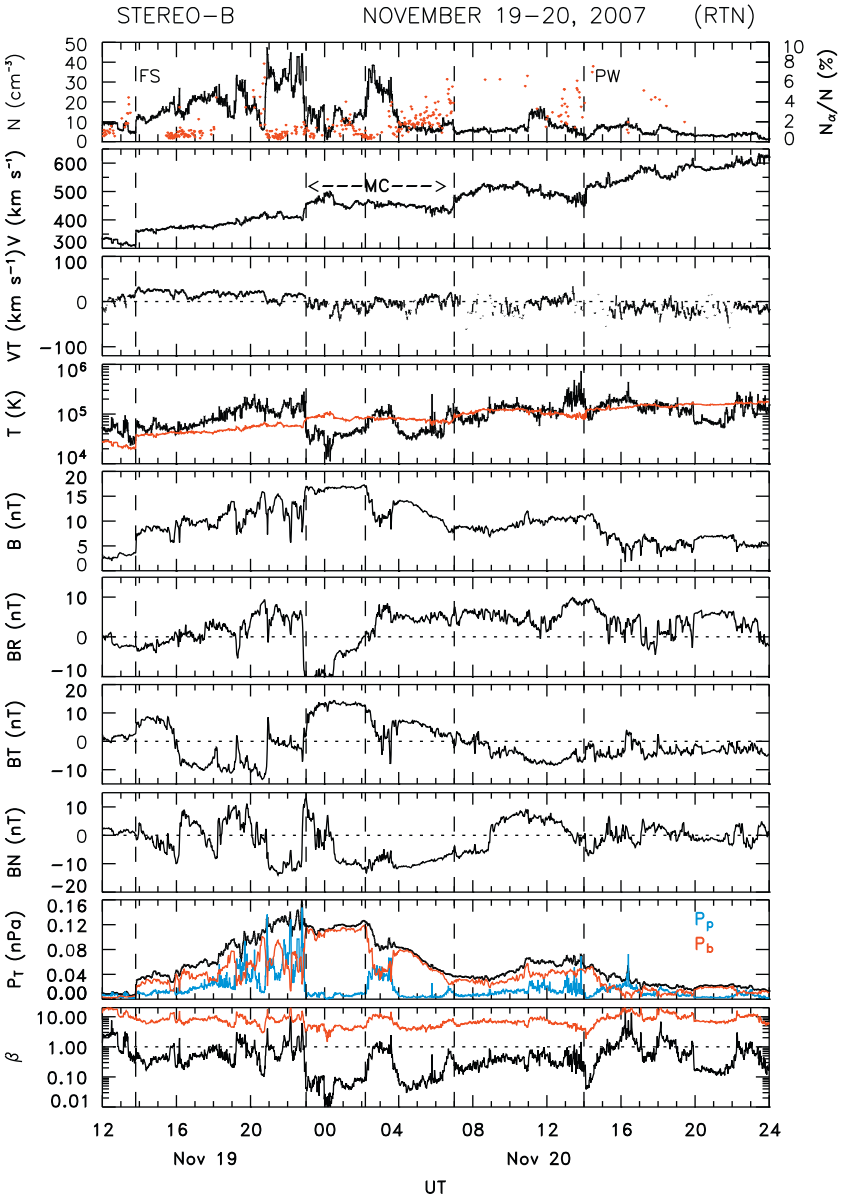

Fig. 2. Plasma and magnetic measurements made by STB during the period 12:00 UT, November 19 to 24:00 UT, November 20. From top to bottom: the proton density (in red: the α particle-to-proton number density ratio in % with scale on the right), bulk speed, the T-component of the velocity vector, temperature, the total field and its components in RTN coordinates, the pressures (total in black, magnetic in red and plasma in blue, and the proton beta (in red: the Alfvén Mach number on the same scale as β). The red trace in panel 4 gives the expected solar wind temperature. (For interpretation of the references to color in this figure legend, the reader is referred to the web version of this article.)

understand a contact discontinuity separating slow from fast winds. At a SI there is usually an abrupt drop in the plasma density coincident with a sharp rise in the proton temperature. The total pressure peaks in the vicinity of the SI. In addition, there are flow shears at the SI, particularly in the east–west flow direction: the slow, dense plasma is deflected westwards while the less dense plasma behind the SI is deflected eastward (i.e. along $-VT$) (see Gosling and Pizzo, 1999, and references therein). In this case, by contrast, there is no deflection in the east–west flow component, VT (panel 3), and other distinguishing features are absent as well.

2.3. Wind

We next turn to Wind observations, shown in Fig. 3 in a format similar to that of Fig. 2. There are some commonalities and also some differences with the observations at STB. (i) The data show a gradual transition from slow to fast solar wind. (ii) There is evidence of a transient: Between $\sim$00 : 20 UT and $\sim$09 : 00 UT, November 20, the proton temperatures and betas are low, the magnetic field strength is higher, and its time profile quieter than average, and the magnetic field vector executes a large rotation. This is thus a MC. It has the same chirality as that at STB, i.e. left-handed. A stream interface, SI, is present as marked. The cloud duration may continue until 11:30 UT, November 20, though the smooth rotation there is disrupted by the encroaching SIR, which probably compressed and warped the trailing part of it. Evaluating the pressure tensor (total momentum flux) it can be shown that as a result of the strong density decrease and the east–west deflection of the flow at the SI (panel 3), tangential stresses are exerted on the MC. If we consider the net changes in the pressures occurring in the period 11:20–12:00 UT, November 20, we find the change in tangential stresses to be $\sim$40% of the change in the normal stresses. The changes are abrupt. Thus, while the compressive forces dominate, the tangential stresses are also significant.

Magnetic field strengths in the MC are somewhat higher than at STB, which may be because spacecraft Wind passes closer to

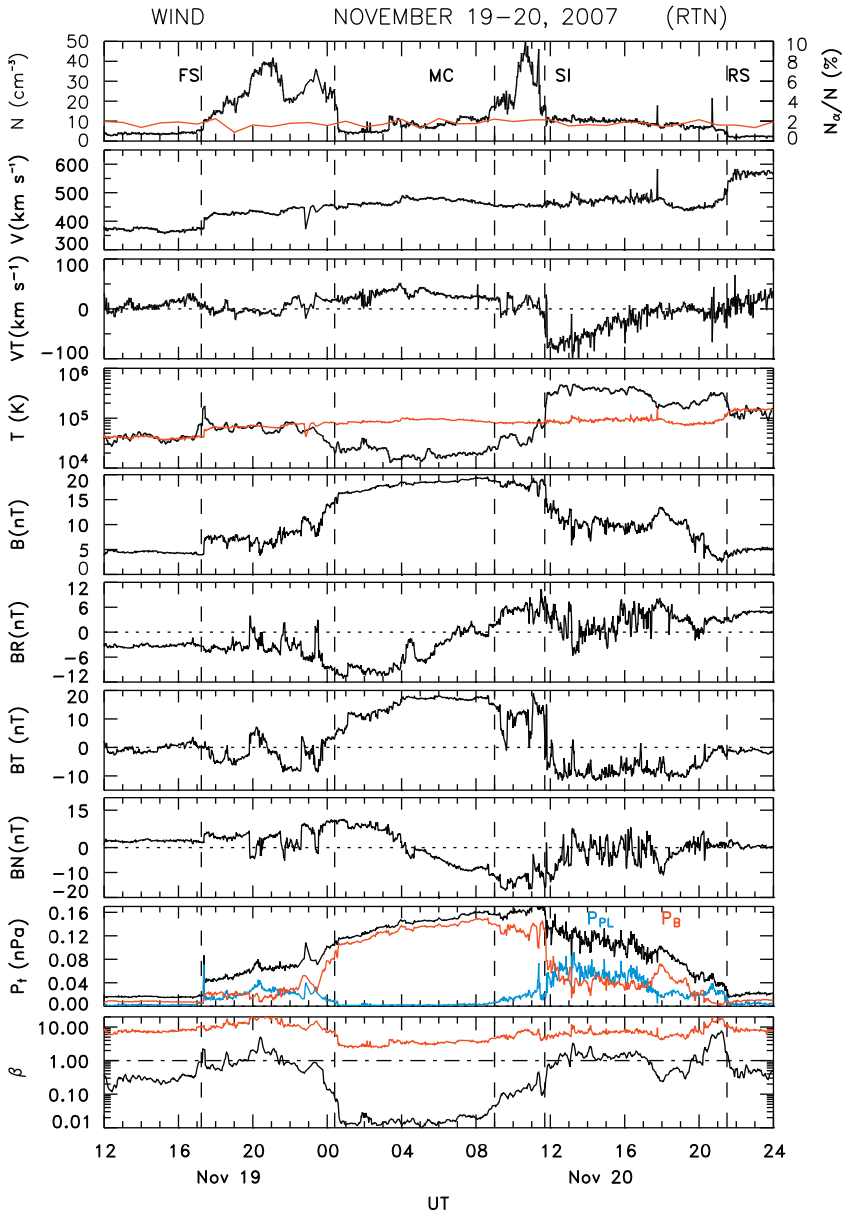

Fig. 3. Similar to Fig. 2 but for Wind. For further details see text.

the cloud axis. At ~21 : 30 UT, November 20, there are indications of a reverse shock (RS). Thus, using 3 s data, we find there are steep decreases in the density, temperature, total field strength and total pressure, and an increase in flow speed. A HCS crossing is indicated in the data since the polarity of the BR component of the field switches from negative on November 19 to positive in the second half of November 20. The transition is smooth and, as noted in other examples (e.g., Crooker and Intriligator, 1996), it appears that the MC has taken on the role of the HCS. We may note that both the FS and the leading edge of the MC arrive at Wind after they do at STB, even though Wind is at smaller heliospheric distance than STB. This might be an indication that the FS is not being driven by the MC at both spacecraft. If it were, one would expect it to arrive at Wind first. The leading edges of the MC at the two spacecraft are separated by ~1.3 h, and the arrival times of the FS are separated by ~3.4 h.

2.4. STA

Fig. 4 shows data acquired by STA, ~20° west of Earth. A longer time interval is plotted, from 12:00 UT, November 19 to 20:00 UT, November 21. A prominent feature of the data is the SI where, in contrast to Wind, the gradients in the bulk speed and temperature are both very sharp. The third vertical guideline indicates the passage of a possible forward shock: the density, total magnetic field strength and total pressure increase but there is hardly any change in the speed and temperature. Alfvénic fluctuations are present in the fast stream behind the SI which, as on STB and Wind, lie in an away sector IMF (BR > 0 nT). The velocity at the start of the interval is higher than at the other spacecraft because STA was still in the trailing edge of the previous high speed stream. The interval 22:00 UT, November 19–20:00 UT, November 20 (between the first two vertical guidelines) is characterized by enhanced field strengths, low proton β and a large rotation of the magnetic field, thus delineating a MC, although its boundaries are somewhat uncertain. It is also left-handed. The cloud is not driving a shock. There are indications of radial expansion in the negative gradient of the flow speed (Klein and Burlaga, 1982; Farrugia et al., 1993). The inferred radial expansion speed is, however, small (~10 km s^{-1}).

We now try to determine the orientation of the MCs using minimum variance analysis of the magnetic field (Sonnerup and

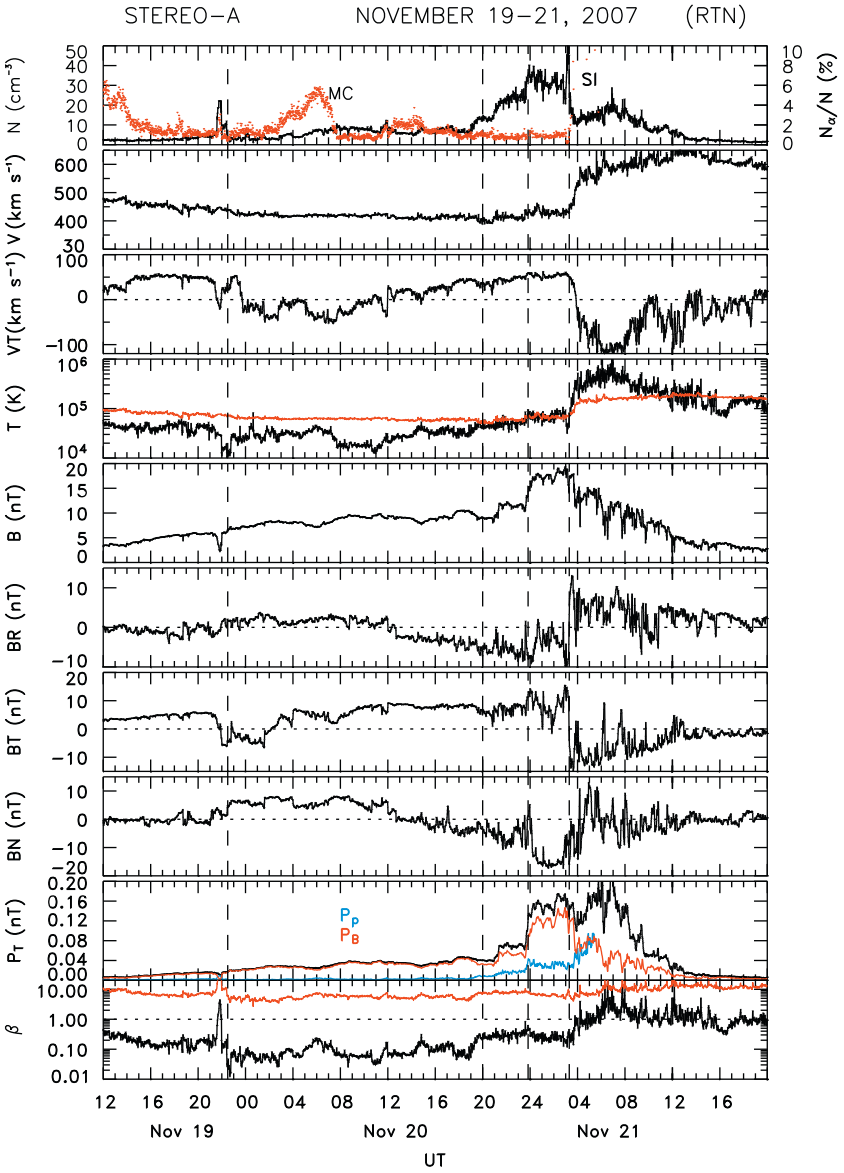

Fig. 4. Similar to Fig. 1 but for STA. A longer time interval is plotted.

Cahill, 1967). In this method, the intermediate eigenvector gives the direction of the cloud axis (Goldstein, 1983).

We examined the following intervals: (i) STB: 23:00 UT, November 19–07:00 UT, November 20; (ii) Wind: 00:20 UT, November 20–09:00 UT, November 20; (iii) STA: 22:30 UT, November 19–20:00 UT, November 20. In all three cases we obtained a very stable result as judged by the ratio of intermediate-to-minimum eigenvalues, λ (=20.0, 7.0, and 9.0, respectively). In RTN coordinates the cloud axes were

$\mathbf{a_{STB}}$: (−0.05, 0.69, −0.72)
$\mathbf{a_W}$: (−0.45, 0.88, 0.13)
$\mathbf{a_{STA}}$: (0.30, 0.78, 0.56)

Had we extended the Wind interval to 11:20 UT, November 20, thus covering the entire interval when $\beta<1$, we would have obtained $\mathbf{a_W}$: (−0.17, 0.98, −0.036) ($\lambda=11.3$), which is inclined by 19.7° to the one quoted above. Before interpreting the results we again draw attention to the fact that the MCs at STB and Wind are certainly being distorted by the trailing, fast stream. Only at STA, if the boundaries are set correctly, is the MC (almost) "pristine". The angles between these axes are 57° (STB-W) (44° for longer Wind interval) 52° (W-STA) (46° for longer Wind interval); and 83° (STB-STA).

Table 1
Results of the MVAR (left) and the force-free fit (FF) model.

	MVAR		FF			
	θ	ϕ	θ	ϕ	B_0 (nT)	p
ST-B	−46.1°	94.1°	−12.5°	12.3°	21.9	0.79
WIND	7.5°	117.1°	−34.4°	68.5°	23.2	0.05
ST-A	34.1°	68.9°	36.1°	61.3°	11.4	0.22

Angle θ is the latitude and ϕ is the longitude (RTN coordinates), increasing toward the T axis. Quantity B_0 is the fitted magnetic field strength at the center of the tube. The impact parameter p gives the closest distance to the center of a tube as a fraction of the radius.

3. Force-free fitting

We now compare our minimum variance results with those obtained from the model of MCs as force-free (FF) configurations to a first approximation, i.e. satisfying $\nabla\times\mathbf{B}=\alpha\mathbf{B}$ (Goldstein, 1983; Marubashi, 1986), with α = constant (Burlaga, 1988; Lepping et al., 1990). Lundquist (1950) obtained a solution for an axially symmetric configuration in a cylindrical geometry (i.e a flux tube of circular cross-section) in terms of Bessel functions of zeroth and first order, J_0, J_1: B_r = 0 (radial), $B_\phi=B_0J_1(\alpha\cdot r)$ (azimuthal), $B_z=B_0J_0(\alpha\cdot r)$ (axial), where B_0 is the model field on the axis, and r is the radial distance from the axis. Clearly, this solution assumes a single flux rope forming the MC, and that the MC is not interacting with surrounding flows, so that the force-free results and their deviation from the GS results given in Section 5 give us a handle on the distortions caused by the interaction.

We employ a least - squares algorithm to fit the model to the data. The routine returns the orientation of the tube, the modeled B_0, and the impact parameter p, i.e. the closest distance each spacecraft passes from the axis. We work with the same intervals as for the minimum variance analysis.

The results are shown in Table 1 and the fits are given in Figs. 5–7 by the red traces. The following points may be made: (i) The best fit is that for STA. (ii) At Wind the FF fit reproduces the BN rotation (normal to ecliptic) well. BR and BT, by contrast, depart substantially from the data, BT in particular reproducing very poorly the almost constant field strength due to compression by the fast stream. (iii) At STB, the variation in BT and BN are reasonably well modeled, while the BR rotation is not. (iv) The impact parameters show that Wind passed closest to the axis of the cloud, and STB passed farthest away. With p=0.79 it is not expected that STB will see the whole structure of the MC. Comparing now with the MVA results (also shown in Table 1), we have agreement in STA results to within 6.4°. The results at STB and Wind are completely different, those at STB departing most from each other. We recall that the MVAR and FF techniques assume (1) a single flux rope, which is (2) of circular cross-section, and (3) not interacting with, and being distorted by, external flows. The GS method presented in Section 5 dispenses with the first two assumptions but retains the third.

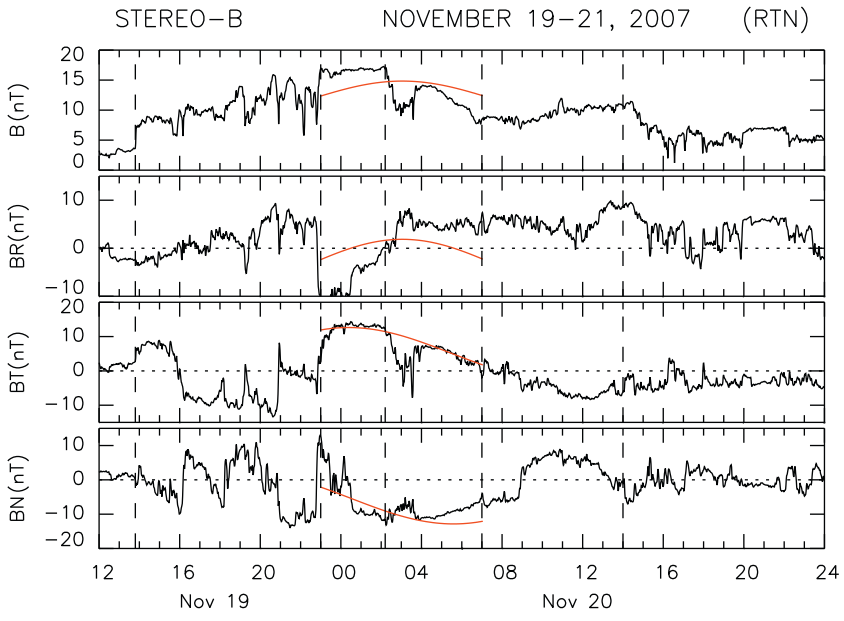

Fig. 5. A least-squares fit of the force-free model to the data (red trace): STB. (For interpretation of the references to color in this figure legend, the reader is referred to the web version of this article.)

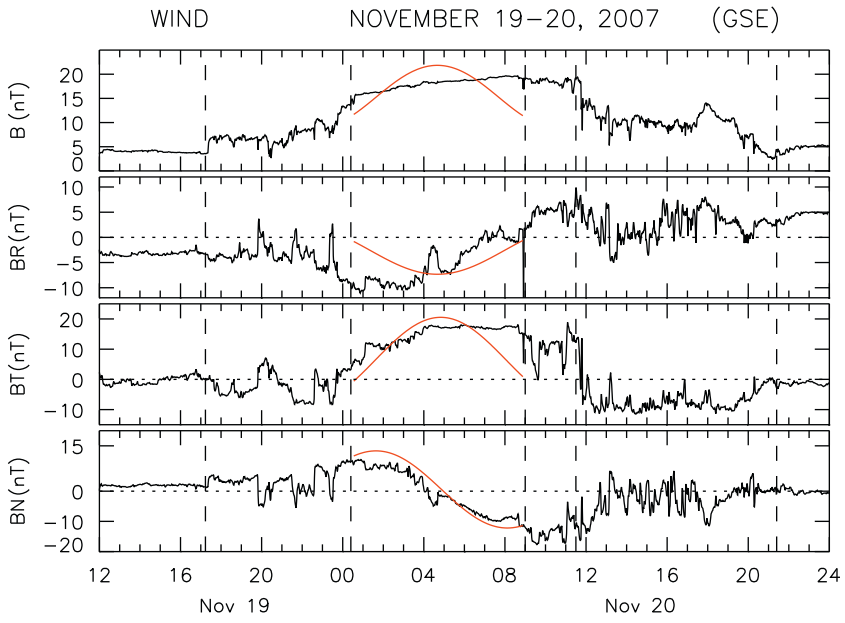

Fig. 6. A least-squares fit of the force-free model to the data (red trace): Wind. (For interpretation of the references to color in this figure legend, the reader is referred to the web version of this article.)

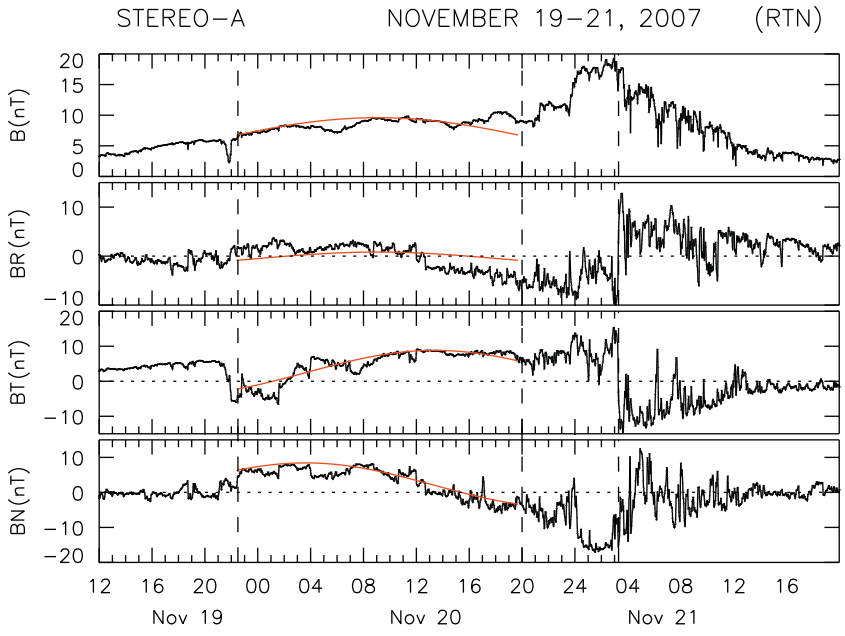

Fig. 7. A least-squares fit of the force-free model to the data (red trace): STA. (For interpretation of the references to color in this figure legend, the reader is referred to the web version of this article.)

Fig. 8 shows these axes directions in two projections, the (RT) (top) and the (NT) planes. MVA results are in blue and FF in red. One clear message emerges from this figure, namely, that the idea of a coherent, single flux tube exhibiting a continuous global curvature is being brought into question by the MVA and FF analyses. We interpret this figure further when we discuss an analogous plot obtained by GS reconstruction in Section 5.

4. Magnetic topology of the transients: the strahl electrons

The non-Maxwellian distribution function of solar wind electrons contains a field-aligned component called the strahl at $E \gtrsim 100$ eV (Montgomery et al., 1968; Ogilvie et al., 1971; Feldman et al., 1975; Pilipp et al., 1987), which carries the heat flux from the Sun. The streaming direction of the strahl has long been used as a tracer of the magnetic topology of MCs/ICMEs (Gosling et al., 1987; Neugebauer and Goldstein, 1997; Crooker and Horbury, 2006). MCs may have "feet" still anchored to the sun, in which case the strahl flows along and opposite to the field, i.e., it is bidirectional. The presence of a unidirectional strahl is often interpreted as indication that only one leg of the ICME is attached to the solar surface and that, for example, reconnection processes at the solar base gave rise to the disconnection (e.g. Gosling et al., 1995). Absence of strahl in an ejecta implies magnetic disconnection, with field lines closing in on themselves in a plasmoid-type configuration.

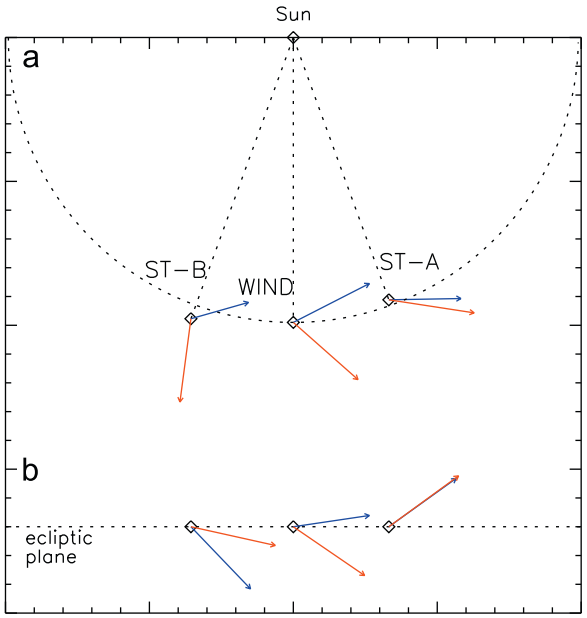

Fig. 8. The orientation of the axis derived from MVA (blue) and FF analysis (red). Figure (a) shows the RT projection while (b) gives the NT projection. (For interpretation of the references to color in this figure legend, the reader is referred to the web version of this article.)

Fig. 9 shows pitch angle distributions (PA) of electrons centered at energy ~250 eV from the SWEA instrument on STB (top) and STA (bottom). The period plotted is from 12:00 UT, November 19 to 18:00 UT, November 21. We discuss STB first. The passage of a plasma sheet during the MC interval results in an isotropization of the flows. (The isotropization of the strahl electrons within the plasma sheet is a characteristic signature [e.g. Crooker et al., 2004].) Otherwise, throughout most of the MC interval there are essentially unidirectional flows, directed opposite to the field. At the back of the cloud, from 06:00–07:00 UT, November 20, there is a brief interval of bi-directionality. From these data we would thus conclude that the MC which encountered STB had only one "leg" connected to the Sun most of the time.

Fig. 10 shows the PA distribution for the strahl electrons centered at 116.1 eV from the Wind/SWE instrument. The period shown is November 19–20, 2007. Flux intensities are color coded. Initially, in the solar wind upstream of the MC, the electrons are flowing along the magnetic field, i.e. antisunward for BR < 0 nT. The PA distributions during the MC interval fall into two categories, temporarily distinct from each other. In the first part (up to about 03:30 UT, November 20), the flows are generally bidirectional, with an excess flux in the antisunward direction. The electron flows then become unidirectional, flowing against the magnetic field (large PA). Between 09:00–12:00 UT, November 20, in the compressed region prior to the SI, there is a complete

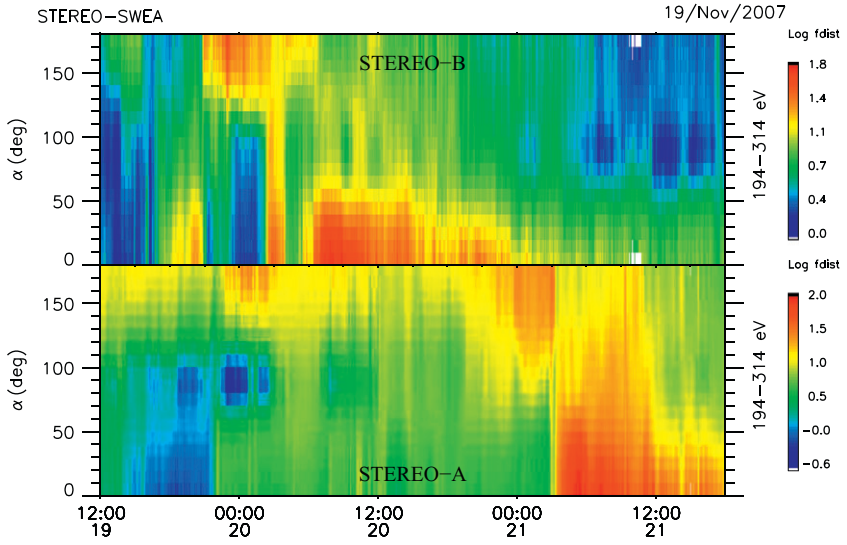

Fig. 9. Electron pitch angle distributions from STB (top) and STA. The energy bin is centered on 250 eV.

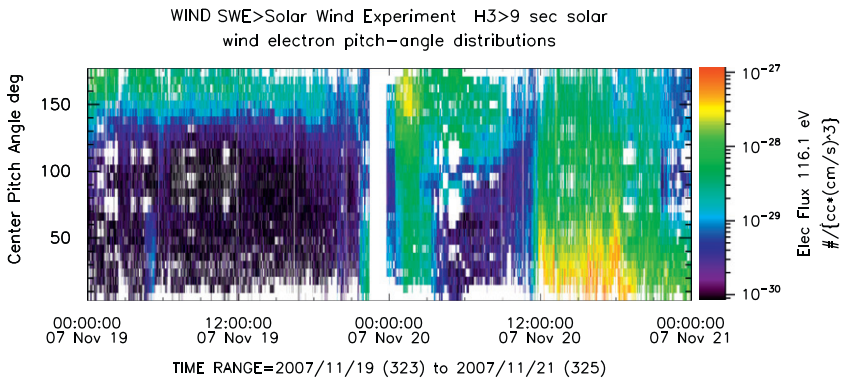

Fig. 10. Spectrogram of pitch angle distributions of ~116.1 eV electrons from the WIND/SWE instrument. The intensity of the electron fluxes is color-coded. The period shown is November 19–November 20, 2007. (For interpretation of the references to color in this figure legend, the reader is referred to the web version of this article.)

dropout of the strahl. The distribution then broadens its pitch angle range, with the fluxes with low PA being very intense. Behind the reverse shock the strahl electrons are flowing mainly along the field.

PA distributions during MC passage are not the same as on STB. This may be due, in part, to the different heliographic latitudes of the probes, making them sample different regions of the MC. On the strength of these Wind data during the MC interval, we can say that either this is a MC which has a mixture of closed and open field lines, as has been found in other examples (see e.g. Shodhan et al., 2000; Gosling et al., 1995), or that it is made up of two flux tubes. Militating against the first possibility is that in previous examples the intervals of counter-streaming suprathermal electrons are either randomly distributed through the MC (Shodhan et al., 2000) or are embedded deep inside the closed field line region (Gosling et al., 1995). By contrast, in the Wind observations they are cleanly separated in time. We return to this topic from a different angle when we discuss the GS reconstruction of the transients at the three spacecraft.

The second panel of Fig. 9 shows PA distributions from STA for the period 12:00 UT, November 19 to 18:00 UT, November 21. The interval starts with flows against the field and ends with flows along the field, as appropriate for the strahl electrons when the magnetic field component BR changes polarity from negative to positive, signifying a HCS crossing. During the passage of the MC (22:30 UT, November 19–20:00 UT, November 20), the flows are bidirectional up to about 12:00 UT, November 20, but with more intense fluxes in the beam moving at large pitch angle to the magnetic field. There is a halo dropout at around 90° PAs at the start of the cloud interval (Gosling et al., 2002). The distribution is generally omnidirectional with what appear to be a few partial drop-outs of the intense, large-pitch angle beam occurring from 08:00 UT, November 20 onwards.

5. Grad–Shafranov reconstruction

We next model the MC observations at the different spacecraft by Grad–Shafranov (GS) reconstruction to see what it tells us about the global structure of this transient. The fact that all three spacecraft observed a MC, and that it had the same chirality, suggest that they crossed part of the same larger structure. We now model the three observations to get quantitative estimates of the global MC parameters and the MC shape.

5.1. Modeling

GS reconstruction (Hau and Sonnerup, 1999; Hu and Sonnerup, 2002) is used to model the MC intervals and thus provide an extended view of the MC's cross-section perpendicular to the MC axis. For an in-depth description of the method we refer the reader to Hu and Sonnerup (2002), Hu et al. (2003) and Möstl et al. (2008, 2009a,b). For our purposes it is only necessary to know that the technique makes two main assumptions: (1) a time-independent structure, which is (2) invariant along a particular direction. For MCs this direction corresponds to the MC axis. An important point is that the technique has its own way of defining the MC boundaries. They are set where the so-called transverse pressure $P_t(A)=p+B_z^2/2\mu_0$, i.e. the sum of the plasma pressure (here we use only protons) and the pressure of the MC axial field component is still a single-valued function of the vector potential A for inbound and outbound measurements through the MC (see Hu and Sonnerup, 2002, Hu et al., 2003). The single-valued constraint on $P_t(A)$ is also used to search for the invariant direction. Magnetic field maps can then be created which show the cross-section of the MC around the spacecraft trajectory. This cross-section is the result of a numerical integration and is thus not prescribed. Another advantage of the technique is its ability to calculate magnetic flux contents within the MC from the deformed cross-sections. The toroidal flux Φ_t is calculated for the surface perpendicular to the MC axis and is associated with the B_z component of the magnetic field along the MC axis in the reconstruction frame. For the poloidal flux Φ_p, the integration surface is taken along the MC axis (for definitions see Qiu et al., 2007).

We now consider evolutionary effects. The spacecraft radial distances from the Sun are the same to within 0.07 AU. The MCs move at $\sim$450 km s^{-1}, which gives a time difference of $\sim$6 h for the given radial separation. Thus we see an almost time-independent snapshot of the MC compared to the transit time ($\approx$100 h for this constant velocity), and so evolutionary effects (Leitner et al., 2007) can safely be ignored. In addition, the expansion speeds, which are defined as half of the difference between the speed of the MC front boundary and that of the back boundary, are small: at STB (STA) the MC expands with $V_{exp}=+15$ (10) km s^{-1}, while at Wind a compression of the MC is underway with $V_{exp}=-7$ km s^{-1}. In summary, the static GS method appears well justified.

We applied this modeling to the MC intervals at all three spacecraft individually. The results are summarized in Table 2, and Fig. 11 shows both the reconstructed magnetic field maps

Table 2
Results of Grad–Shafranov reconstruction for each spacecraft.

Spacecraft	STB	Wind	STA
R_{sun}, AU	1.0384	0.9781	0.9655
D_{sheath}, AU	0.0856	0.0802 AU	–
MC front, UT	November 19 23:14	November 20 00:58	November 19 22:29
duration, h	7:25 h	7:20 h	14:10 h
$\|V_{HT}\|$, km s^{-1}	444	472	424
B_z, nT	15.9	18.7	9.7
θ, deg	−40	2	35
ϕ, deg	110	122	47
H	L	L	L
D, AU	0.077	0.074	0.166
p, %	0.07	0.20	0.05
Φ_t, 10^{21} Mx	0.05	0.15	0.17
Φ_p, 10^{21} Mx/AU	0.25	0.47	0.64
I_z, MA	230	244	302

D_{sheath} is the size of the sheath region between the shock and magnetic cloud (MC) front boundary as described in the text. Parameter θ is the inclination to the RT plane (close to the solar equatorial plane); ϕ is measured from R towards T; B_z is the axial field strength; $|V_{HT}|$ is the de Hoffmann–Teller velocity; D is the radial scale size, which is defined as the length of the spacecraft trajectory through the MC perpendicular to the axis (equal to the length of x′ in Fig. 11; p is the impact parameter, the closest approach of the spacecraft to the MC axis, and given as a fraction of D; The magnetic fluxes and the axial current I_z are calculated for the domains inside the white boundaries in the magnetic field maps in Fig. 11.

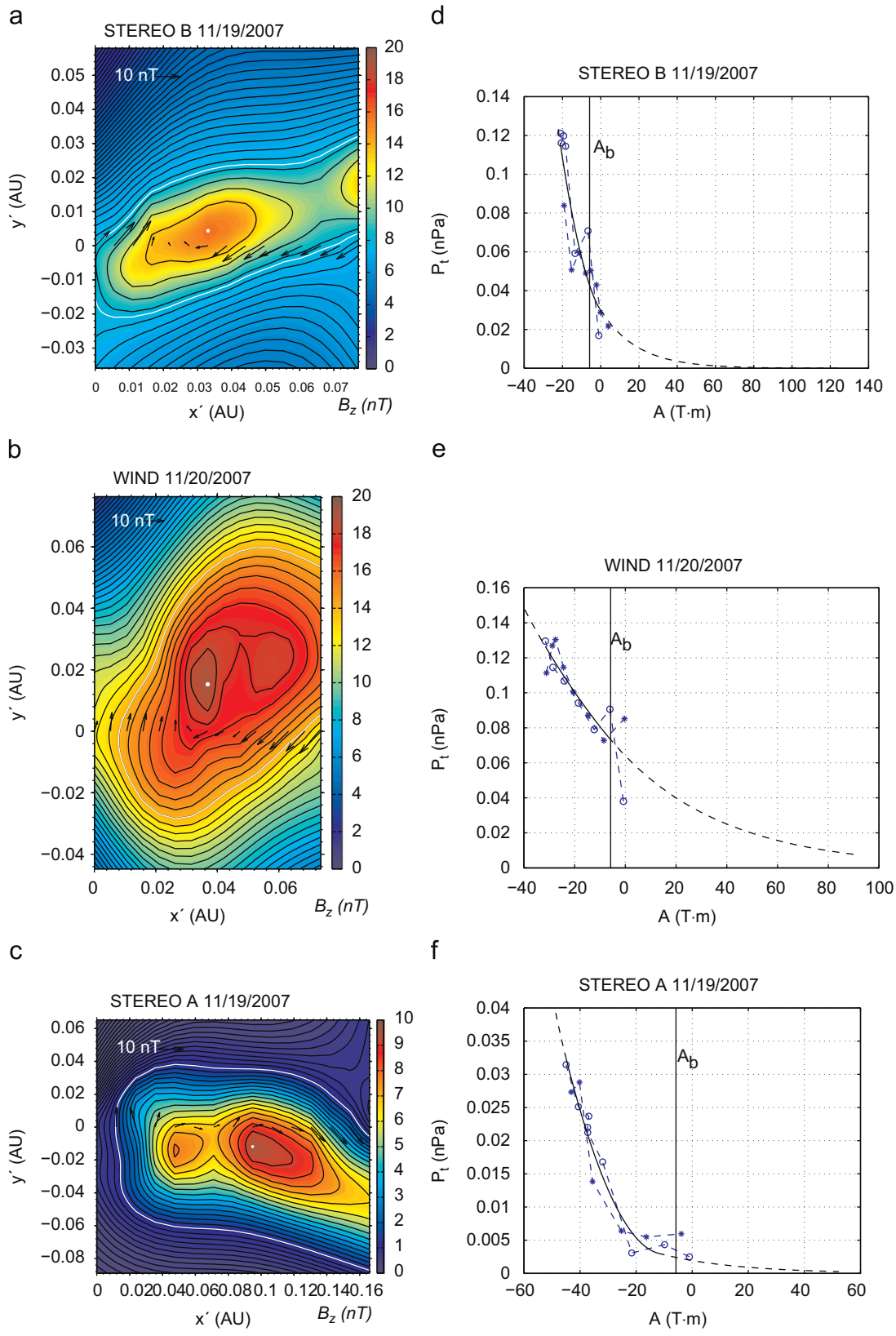

Fig. 11. (a–c) Magnetic field maps obtained from Grad–Shafranov reconstruction from solar east to west: STB (a), Wind (b) and STA (c). Black contours are transverse magnetic field lines, the B_z component (color-coded) is pointing out of the paper. (d–f): $P_t(A)$ function derived from observations (dashed blue) and fitted by a 2nd order polynomial (solid black). This is used for integration of the Grad–Shafranov equation to obtain the magnetic field maps on the left. Circle (star) symbols indicate inbound (outbound) measurements. The vertical lines are drawn at a value of $A = A_b$ where the inbound and outbound data diverge. (For interpretation of the references to color in this figure legend, the reader is referred to the web version of this article.)

(to the left) and the fitted $P_t(A)$ functions (to the right) used for the numerical integration. The maps on the left show the recovered magnetic field structure transverse to the axis. The reconstruction coordinate system (x′,y′) is as defined in Hu and Sonnerup (2002). The black contours represent magnetic field lines transverse to the axis. The strength of the axial field, B_z (pointing out of the plane of the paper) is color-coded. It maximizes at the white dot. The thick white contour line is drawn at a value $A_b = -5$ nT (see below). Black arrows along the spacecraft trajectory are the projections of the measured field into the (x',y') plane.

For each spacecraft, the plots on the right show P_t as a function of A. Scattered points joined by a dashed blue line are the observations—circled (starred) symbols indicate inbound (outbound) measurements. They are fitted with a second order polynomial (solid black trace). The latter demonstrates that $P_t(A)$ is indeed single-valued for (in this case) small values of A. This is used to integrate the GS equation and obtain the maps shown on the left. The vertical lines drawn at a values of $A_b = -5$ nT correspond to the white contour in the field maps on the left and indicate the boundary of the MC as determined by the GS method.

Significantly, the reconstruction method yields double-flux ropes at STA and Wind, and a single flux rope at STB, where the second rope might have been missed by the spacecraft (Fig. 11(a)). We note that MCs with a double-flux rope structure have been discussed by Hu et al. (2003).

We summarize first the similarities between the different reconstructions:

1. The velocities are the same to within 50 km s^{-1}.
2. The expansion is negligible at all three spacecraft.
3. The impact parameters are low everywhere, ranging from 5% to 20% of the radial scale size (largest at Wind).
4. The orientation points roughly to solar west (positive RTN-T).
5. The axial currents are about the same at all three spacecraft.

The main differences we find are:

1. The radial scale size D at STA is 2–2.5 times larger than at the other two spacecraft.
2. The axial magnetic field is similar at STB and Wind, at about twice its value at STA.
3. Both axial and poloidal magnetic fluxes are the same at Wind and STA, and equal roughly to twice of the value at STB.
4. Concerning the shape of the cross-section, from the GS maps (Fig. 11) it follows that at Wind the shape is more “compressed”, i.e. elongated along y', which is perpendicular to the approximate direction of motion (x') at Wind. In contrast, at STA and STB it is more elongated in the direction of motion, consistent with the interpretation that the compression by the SIR is just underway as the structures pass Wind.

Comparing the orientations obtained here with those from MVA, we find, perhaps surprisingly, good agreement. Thus the angles between the axes as determined by GS and MVA are: 13° (STB), 8° (Wind), and 18° (STA). In summary, then, it becomes clear that at 40° separation and for this particular event, we see a more complex situation than a simple coherent flux rope at three points in space. This is already clear from the previous sections. We now ask, how can the differences and similarities concerning the global structure of the MC be reconciled?

5.2. Discrepancies in the magnetic fluxes

First, it stands out that the magnetic fluxes at STB are significantly less than those at the other two spacecraft (Table 2). In view of the fact that the flux ropes are still distinct, the most likely interpretation seems to us to be the following: At STB, the impact parameter is much higher for the second flux rope so that the reconstruction using STB data misses it and we calculate only roughly half of the magnetic flux in the magnetic field map as compared to the other two reconstructions. In this case the helical magnetic fields and the magnetic flux could be coherent over 40° longitudinal separation. Because 40° correspond to ≈ 0.7 AU along a circle, this would give us a lower limit of the MC axial length of $L = 0.7$ AU (see also Yamamoto et al., 2010).

5.3. Global MC shape

Fig. 12 shows a sketch of the flux tube orientation at the 3 locales. This plot corresponds to the time when Wind encounters the MC's front boundary at 00:58 UT, November 20, 2007, which serves as the time of reference. The MC front boundaries at STA and STB were seen 149 min (A) and 104 min (B) earlier than at Wind, respectively. In Fig. 12 the front boundaries of the MC have thus been displaced with respect to the spacecraft position assuming a radial propagation from the Sun with a constant velocity (cf. Burlaga et al., 1981, Figure 5), which is in our framework the de Hoffmann–Teller velocity, V_{HT}. Note that V_{HT} is approximately equal to the average speed over the respective MC intervals. Also the positions of the shocks at STB and Wind are indicated. The size of the cloud sheath at Wind, and the distance between the shock and the first MC front boundary at STB, have been calculated by $S_{sheath} = \sum_i V_i \times \Delta t_i$. This yields for Wind $S_{sheathW} = 0.0802$ AU and for STB $S_B = 0.0856$ AU. Now, the respective distances S_{sheath} has been added to the MC front boundary positions at STB and Wind along the radial direction from the Sun to indicate the shock position. To approximately show the global MC front boundary, a green line connects these positions. This yields an almost straight line. Furthermore, a line connecting the shock positions (yellow) is parallel to the estimated front boundary shape.

The flux rope orientations in Fig. 12 are obviously inconsistent, particularly their inclinations to the ecliptic, which change from −40°, thus pointing southward at STB, to 2° at Wind and to +35°, thus pointing northward at STA. (See also the MVA results in Fig. 8 [blue arrows].) At the present stage, it is not clear if the model assumption of invariance might be violated and the GS method might give a wrong picture, or if this really reflects a very different flux rope orientation along the MC axis. However, it is certainly inconsistent with the classic picture of MCs as huge bent flux ropes having one particular inclination to the ecliptic which is valid on a global scale. From Fig. 12 it follows that the MC front boundary is unexpectedly not a loop but rather a straight line. If one takes into account the different orientations of the local MC axes, a kind of warped MC shape emerges which is shown by connecting the axes in the upper panel of Fig. 12. As noted above, the MC shape is likely to have been influenced by the interaction with the trailing high speed stream.

Finally, we note that the lower limit on the MC's longitudinal extent in the ecliptic of 40°, as given by the separation of the STEREO probes, is consistent with the 60° upper limit for this quantity given by Bothmer and Schwenn (1998).

6. Analysis of the shocks

We calculate the shock normal by three methods: velocity coplanarity, magnetic coplanarity, and the mixed method of Abraham–Schrauner, with the added constraint that at least two of the methods should yield the same normal within a few degrees (see Berdichevsky et al., 2000). We start the shock analysis by searching in a time series plot for a time-aligned discontinuity in plasma and magnetic field parameters of the fast

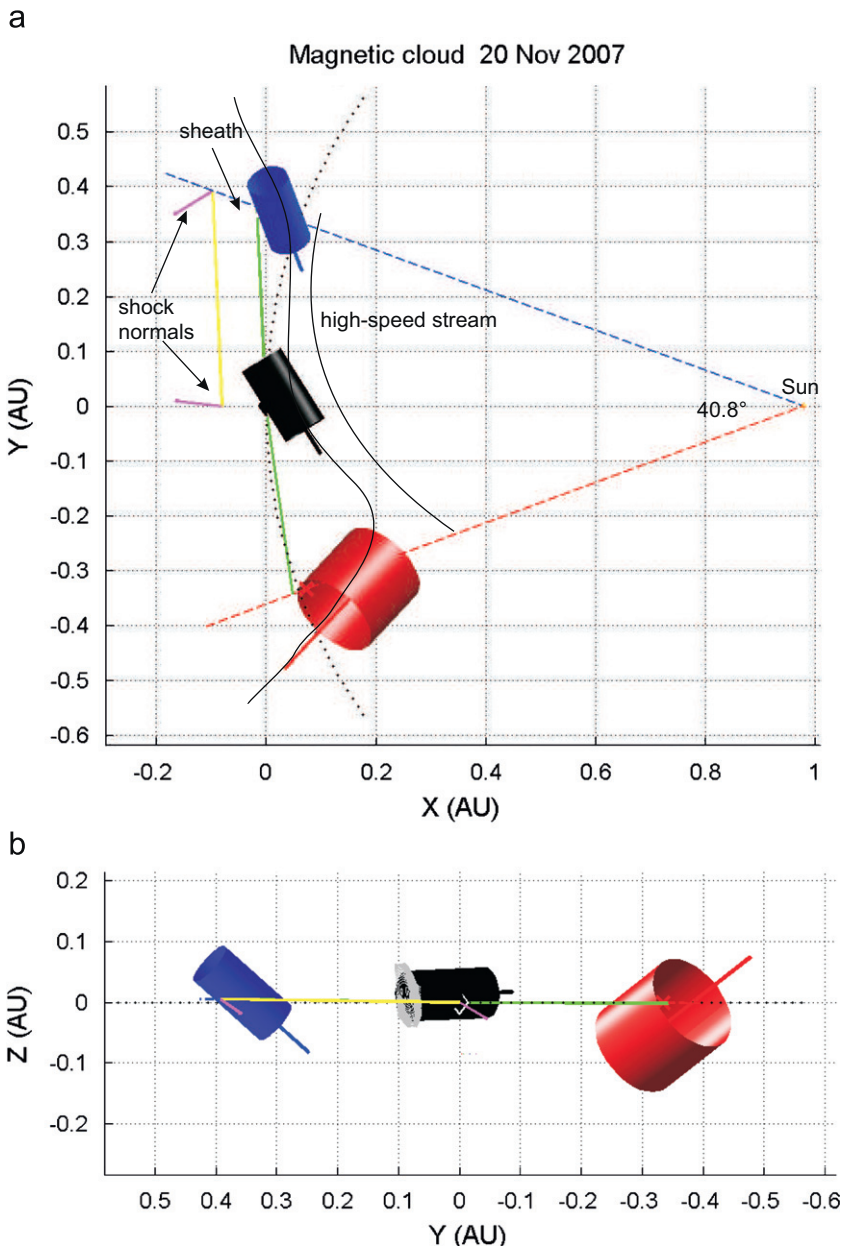

Fig. 12. Sketch of the MCs global shape. (a) Looking down onto the ecliptic from ecliptic north in a solar ecliptic coordinate system (SE) centered on Wind. The blue cylinder indicates the size and orientation of the MC at STB, the black cylinder at Wind, and the red cylinder at STA, assuming zero impact parameters. The green line connects the MC front boundary locations corrected for the timing difference (see text). The yellow line connects the shock locations. (b) The same seen in the SE *YZ* plane looking toward the Sun (along +*X*). (For interpretation of the references to color in this figure legend, the reader is referred to the web version of this article.)

interplanetary shock type (see e.g., Berdichevsky et al., 2000, Figures 1 and B, parts (a) and (b)). We then search near the shock ramp for the regions upstream/downstream of the shock that are most consistent with their belonging to the same magnetic plasma domain upstream/downstream of the shock compression. Having identified the upstream/downstream regions, we evaluate the shock normal, its error, and the velocity of propagation in the interplanetary medium as shown for "The p-ave Technique" (Berdichevsky et al., 2000, Appendix A1) in such a way that the shock solution is sturdy and gives the best solution consistent with the Rankine-Hugoniot equations (see Berdichevsky et al., 2001). The results obtained are listed in Table 3.

At STB: Several hours ahead of the MC there is in the observer frame (RTN coordinates) a fast forward interplanetary shock moving at a speed of 390 km s^{-1} and oriented 12° westward. The direction of this shock is consistent with its being driven by the high speed stream observed later, on November 20. There are two reasons for dismissing the shock as one being driven by the MC: (i) the shock speed $\ll$450 km s^{-1}, the MC's leading speed, and (ii) the orientation of the MC axis appears to be oblique to the shock normal, in contrast to well-known cases of shocks driven by MCs (see e.g., Lepping et al., 2001).

At wind: Ahead of the MC there is a fast forward interplanetary shock moving at a speed of 450 km s^{-1} radially away from the sun. This shock appears to be driven by the MC because (i) its velocity is the same as that of the MC's leading edge, and (ii) the shock orientation is orthogonal to orientation of the MC axis, supporting the idea that the upstream solar wind is pushed as the MC displaces itself as a whole away from the sun, consistent with the interpretation in other studies (see e.g., Lepping et al., 2001).

The arrival of the high speed stream is accompanied by the presence of a fast reverse interplanetary shock. This relatively

early appearance of the reverse shock after the SI may be related to the ongoing building of a complex MC—high speed stream interaction in the inner heliosphere. However, it is not too unusual to find fast reverse interplanetary shocks at 1 AU between a slow and a fast stream, as they have been observed relatively often in the past (see e.g., Berdichevsky et al., 2000). Studying SIRs at 1 AU during 1995–2004, Jian et al. (2006) find that about 6% of them have only a reverse shock.

At STA: There is a relatively quick transition from the MC to the high speed stream. There might have been a forward shock preceding the SI but, as noted in Section 2.4, we believe the evidence for this is inconclusive.

7. Elements of geoeffective response

We now discuss briefly aspects of the geomagnetic disturbances caused by this MC–CIR complex. In this case the magnetosphere is under the influence of two interplanetary triggers which partly overlap. They are the sustained $B_z < 0$ nT phase in the second part of the MC, and a magnetic field which fluctuates about a negative average B_z (mean $= -4.2$ nT) after the SI. As a general comment, we note in passing that the Alfvén Mach number in the magnetic cloud was low (~ 3) and this will affect the response of the magnetosphere in many ways (see Lavraud and Borovsky, 2008).

Table 3
Results from the shock analysis.

SC/UT	Day	S type	**N**	Thet (B.n) (deg)	Shock V (RH-frame)	RTN	Mach nos.
B/13:45	19	FS	(0.800 0.56 −0.23)	62	(74 52–21)	(380 83 −30)	3.0/1.7
W/17:22	20	FS	(0.938 −0.11 0.33)	51	(64.5 −9 22)	(453 −10 22)	1.7/1.1
W/21:32	20	RS	(−0.927 −0.01 −0.36)	18	(−104 1 −44)	(405 6. −82)	2.2/1.5

The columns show from left to right: spacecraft, UT in hh:mm, and date in month/day, shock type, shock normal components in RTN coordinates, the angle between the upstream field orientation and the shock normal, the shock velocity (RTN) in a frame moving with the upstream solar wind, and the shock velocity in the stationary heliospheric frame. The last column shows the shock Alfén Mach and Magnetosonic Mach numbers.

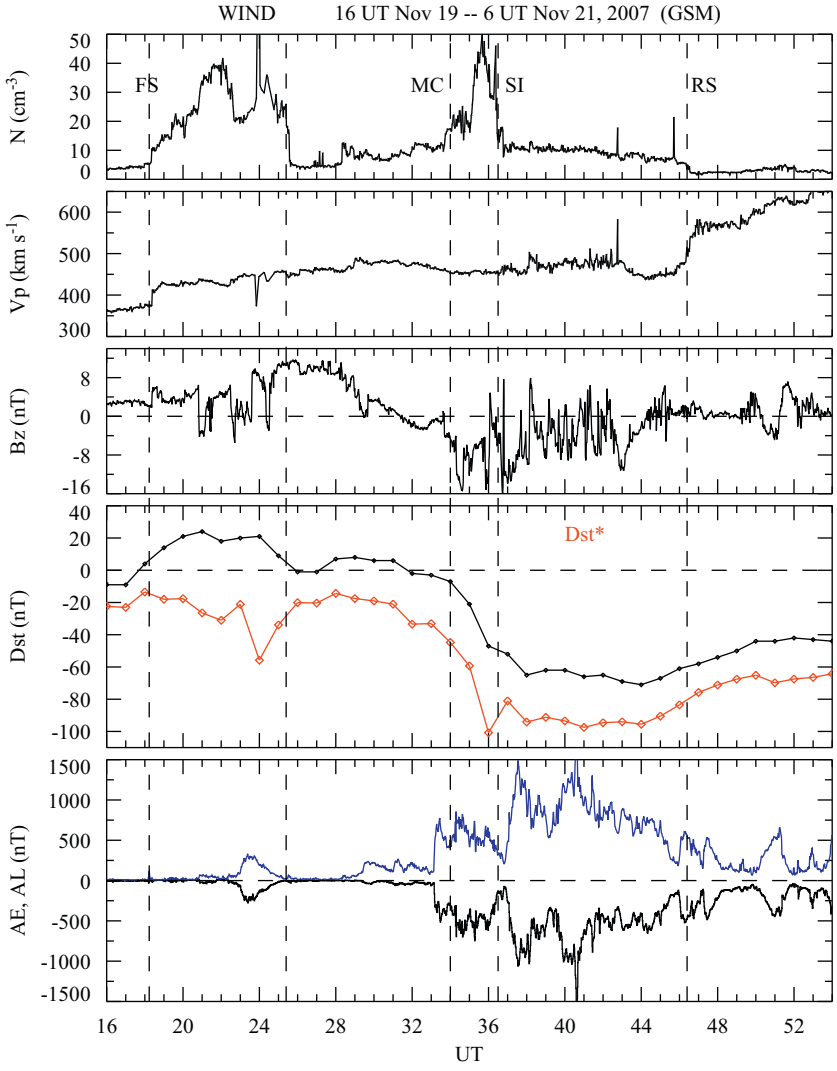

Fig. 13. For the interval 16:00 UT, November 19 to 6:00 UT, November 21, the panels show the proton density, bulk speed and GSM B_z component of the magnetic field at Wind, the Dst index (in red: corrected for magnetopause currents); and the AE (in blue) and AL auroral indices. (For interpretation of the references to color in this figure legend, the reader is referred to the web version of this article.)

The fluctuations in high speed streams are often thought to be Alfvénic in nature. To check this, we consider the interval 13:00–18:00 UT, November 20. We take 3 s Wind data, subtract a running 1-min average to obtain the fluctuations, and check if the residuals in the **B** and **V** vectors ($\Delta B_{x,y,z}$, $\Delta V_{x,y,z}$) are related by $\Delta B_{x,y,z} \sim (n_p)^{1/2} \cdot \Delta V_{x,y,z}$, where n_p is the proton number density. Over 6000 data points the correlation coefficients are $-0.75(x)$, $-0.65(y)$, $-0.65(z)$, respectively, which gives a confidence level above 99.9%. The slopes are $-0.91(x)$, $-0.74(y)$, $-0.88(z)$, indicating Alfvén waves propagating in the direction of the magnetic field.

Fig. 13 shows in the last two panels indices of geomagnetic disturbances, namely, the storm-time Dst index (dark trace) and the auroral AL and AE (in blue) indices. The Dst index is corrected for Chapman–Ferraro (magnetopause) currents, following Burton et al. (1975), and is shown by the red trace. The first three panels include the proton number density, bulk speed and the GSM B_z component of the magnetic field for reference. Vertical guidelines indicate identified regions and discontinuities as in Fig. 3. The Wind times have been shifted by 1 h to take account of propagation delays. The Dst data is at 1 h resolution while the auroral electrojet indices are at 1 min resolution. Both are from the University of Kyoto website.

The following points are worth noting. The interaction led to a (borderline) major geomagnetic storm (Dst < -100 nT). The duration of the Dst profile at minimum values is protracted. There are signs even in this (low) resolution of a double-dip storm, i.e. the Dst goes first to a minimum, recovers somewhat, and then decreases to a second minimum. We recall that over a large survey Kamide et al. (1998) concluded that $\sim 67\%$ of major storms were of the two-step type and suggested a superposition of triggers as the cause of this. Here we have one example. Another example of superposition of triggers leading to two-step major storms are ICME mergers (Berdichevsky et al., 2003; Farrugia and Berdichevsky, 2004; Farrugia et al., 2006). The interaction has obviously prolonged the duration of peak-storm intensity phase. Periodic substorms (Borovsky et al., 1993; Farrugia et al., 1993) may be noted at the sudden dips in the AL-index. The interval is too short to distinguish the periodicities during MC and fast stream passage. A delay of ~ 3 h may be seen between the onset at hours 36.5 and 39.5, lying somewhere between the statistical periodicities during continuous negative B_z in ICMEs (2–3 h) and CIRs (~ 4 h) (Morley et al., 2009, and references therein).

We recall from the Introduction that Burlaga (1975) showed that the formation of a compound stream, such as we have here, tends to enhance the geomagnetic activity. To get a feel for the geoeffects of the interaction, we plot in Fig. 14 similar data but taken about a month earlier. On October 25, i.e. 26 days earlier,

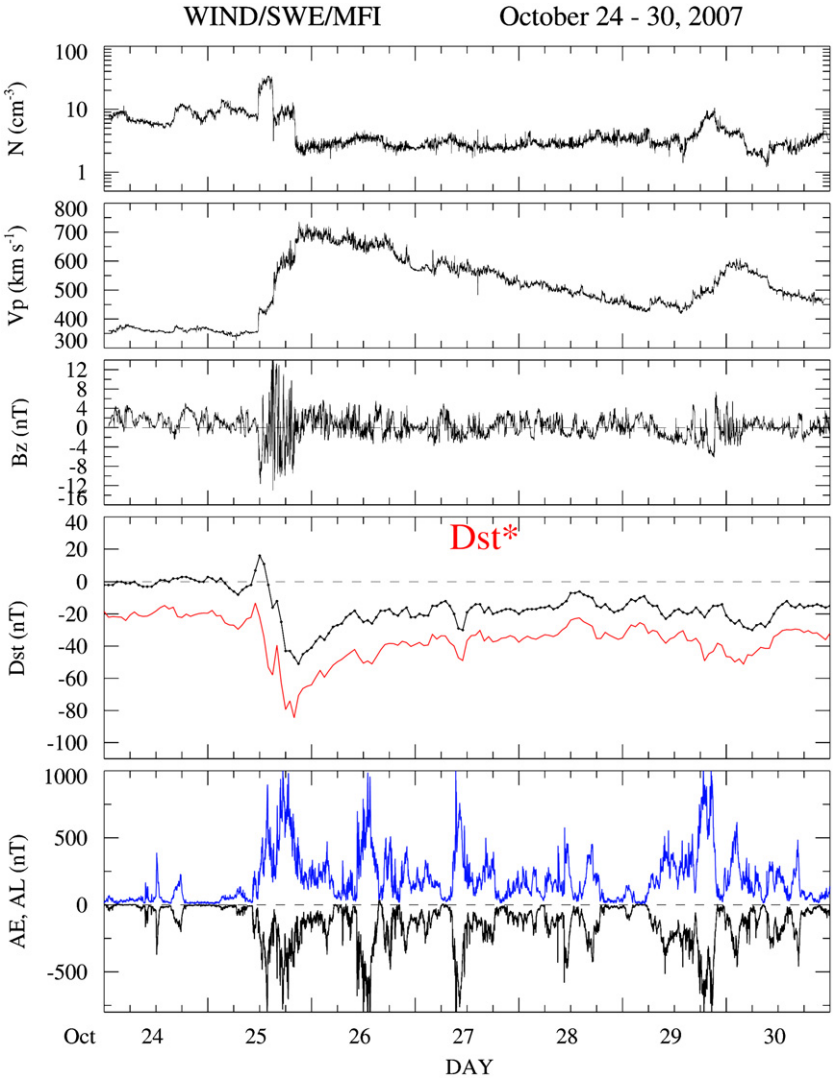

Fig. 14. Similar data as the previous figure but for the 7-day interval October 24–October 30, 2007. The same CIR as in the previous figure but one solar rotation earlier.

the same CIR is seen. Here the corrected Dst reached −80 nT. The continued auroral activity over several days is evident from the last panel. These are the so-called HILDCAAs for high-intensity long-duration continuous AE activity (Tsurutani and Gonzalez, 1987).

Note that Dal Lago et al. (2002) showed that the peak Dst can be intensified from −60 to −100 nT by virtue of the interaction between a MC and an overtaking high speed stream. They studied two cases of MCs being overtaken by, and interacting with, two high speed streams. Our findings are consistent with this result.

8. Summary and conclusions

We have discussed plasma and magnetic field observations made near 1 AU of an interaction between a MC and a CIR. The data were returned by three spacecraft (STB, Wind, STA) situated near 1 AU with a large spread in the heliographic longitude ($\sim 40^{\circ}$) and a smaller separation in heliographic latitude ($\sim 5^{\circ}$). This is one of the few examples in the literature of a MC being observed by three spacecraft at an azimuthal separation which is close to the maximum statistical width of MCs. A corotating interaction region was also clearly observed at all three spacecraft. As expected, we found distortions and rotations of the MC at STB and Wind, as inferred, for example, from the temporal profiles and the disagreement in the axis orientations inferred from three independent methods. By contrast, the methods of determining the axis agreed quite well when applied to STA data.

From the GS reconstruction technique described here we infer a double-flux rope MC structure. It suggests that coalescence between the two flux tubes was still ongoing at the time when the MC reached 1 AU. The presence of two flux tubes at Wind and STA was not well reproduced at STB. This is, we believe, an impact parameter effect, i.e. STB passed too far from the axis of the second flux rope. Consistent with this was the discrepancy we found in the magnetic fluxes, where those at STB were much less than those at WIND and STA, which were comparable. As regards the global shape of the MC, we found that its front boundary is not a (convex outward) loop but resembled rather a straight line.

At Wind there was a clear reverse and forward shock pair. Cases of a forward and reverse shock pair caused by an over-expansion of ICMEs have been reported in the literature (Gosling et al., 1998). This is, however, not such a case because the clouds were hardly expanding at all. From the shock analysis it emerged that the forward shock at STB was driven by the fast stream, while that at Wind was likely driven by the MC.

As regards the geomagnetic disturbances, we showed that this interaction intensified the ring current energization and led to a major storm (Dst ≤ -100 nT) when the effect of magnetopause currents—which were considerable in this CIR-induced compression—were included. Further, it lengthened substantially the duration of maximum solar wind forcing of the magnetosphere (duration of minimum Dst). As regards the Dst time profile, we noted (using 1-hour averages) a tendency for a two-step storm to develop, when Dst drops to a first minimum, recovers somewhat, and then decreases to a second minimum. The interplanetary causes of "double-dip" storm—and about 67% of major storms are of this variety (Kamide et al., 1998)—are clear: the negative B_z interval in the second part of the MC followed by the Alfvénic waves containing a B_z component fluctuating around −4 nT. So CIR–MC interactions are another source of the two-step geomagnetic storms so common in the statistics of Kamide et al. (1998).

The example we examined was complex and it was only the availability of STEREO and L1 monitors which made this study possible. This is different than having just one orbit through a large structure. With one spacecraft we would hardly have done justice to what is really happening at 1 AU. Even so, it had aspects which are hard to interpret and remain somewhat speculative.

Acknowledgements

Our special thanks go to the referees for their many helpful comments. We thank Robert P. Lin and Ronald P. Lepping for the use of Wind 3DP and MFI data, taken from NASA's cdaweb site. We also thank the University of Kyoto website for the geomagnetic indices. This work is supported by NASA Grants NNX08AD11G, NNX10AQ29G, and STEREO Grant NAS5-03131.

References

Acu na, M.H.D., Curtis, J.L., Scheifele, C.T., Russell, P., Schroeder, A., Szabo, J.G., Luhmann, 2008. The STEREO/IMPACT magnetic field experiment. Space Sci. Rev. 136 (1–4), 203–226.

Berdichevsky, D., Szabo, A., Lepping, R.P., Viñas, A.F., Mariani, F., 2000. Interplanetary fast shocks and associated drivers observed through the twenty-third solar minimum by wind over its first 2.5 years. J. Geophys. Res. 105, 227–289.

Berdichevsky, D., Szabo, A., Lepping, R., Viñas, A., Mariani, F., 2001. Correction to: "Interplanetary fast shocks and associated drivers observed through the 23rd solar minimum by Wind over its first 2.5 years" by D.B. Berdichevsky, et al. J. Geophys. Res. 106, A11, doi:10.1029/2001JA000074.

Berdichevsky, D.B., Farrugia, C.J., Lepping, R.P., Richardson, I.G., Galvin, A.B., Schwenn, R., Reames, D.V., Ogilvie, K.W., Kaiser, M.L., 2003. Solar–heliospheric–magnetospheric observations on March 23–April 26, 2001: similarities to observations in April 1979. In: Velli, M., Bruno, R., Malara, F. (Eds.), Solar Wind 10, CP-679. AIP Conference Proceedings, vol. 679, pp. 758–761.

Borovsky, J.E., Nemzek, R.J., Belian, R.D., 1993. The occurrence rate of magnetospheric-substorm onsets: random and periodic substorms. J. Geophys. Res. 98, 3807–3813, doi:10.1029/92JA02556.

Bothmer, V., Schwenn, R., 1998. The structure and origin of magnetic clouds in the solar wind. Ann. Geophys. 16, 1–24.

Burlaga, L.F., 1975. Interplanetary streams and their interaction with Earth. Space Sci. Rev. 17, 327–352.

Burlaga, L.F., 1988. Magnetic clouds and force-free fields with constant alpha. J. Geophys. Res. 93 (A7), 7217–7227.

Burlaga, L.F., 1995. Interplanetary Magnetohydrodynamics, International Series on Astronomy and Astrophysics. Oxford University Press, New York.

Burlaga, L.F., Sittler, E., Mariani, F., Schwenn, R., 1981. Magnetic loop behind an interplanetary shock: voyager, Helios and IMP 8 observations. J. Geophys. Res. 86, 6673–6684.

Burlaga, L.F., McDonald, F., Goldstein, M., Lazarus, A., 1985. Cosmic ray modulation and turbulent interaction regions. J. Geophys. Res. 90 (A12), 12027–12039.

Burlaga, L.F., Behannon, K.W., Klein, L.W., 1987. Compound streams magnetic clouds, and major geomagnetic storms. J. Geophys. Res. 92, 5725–5734.

Burlaga, L., Berdichevsky, D., Gopalswamy, N., Lepping, R., Zurbuchen, T., 2003. Merged interaction regions at 1 AU. J. Geophys. Res. 108, 1425, doi:10.1029/2003JA010088.

Burton, R.K., McPherron, R.L., Russell, C.T., 1975. An empirical relationship between interplanetary conditions and *Dst*. J. Geophys. Res. 80, 4204–4214.

Crooker, N.U., Intriligator, D.S., 1996. A magnetic cloud as a distended flux rope occlusion in the heliospheric current sheet. J. Geophys. Res. 101, 24343–24348.

Crooker, N.U., Huang, C.L., Lamassa, S.M., Larson, D.E., Kahler, S.W., Spence, H.E., 2004. Heliospheric plasma sheets. J. Geophys. Res. 109, A03107, doi:10.1029/2003JA010170.

Crooker, N.U., Horbury, T.S., 2006. Solar imprint on ICMEs their magnetic connectivity and heliospheric evolution. Space Sci. Rev. 123, 93–109.

Dal Lago, A., Gonzalez, W.D., de Gonzalez, A.L.C., Viera, L.E.A., 2002. Stream-interacting magnetic clouds causing very intense geomagnetic storms. Adv. Space Res. 30 (10), 2225–2229.

Davis, C.J., Davies, J.A., Lockwood, M., Rouillard, A.P., Eyles, C.J., Harrison, R.A., 2009. Stereoscopic imaging of an Earth-impacting solar coronal mass ejection: a major milestone for the STEREO mission. Geophys. Res. Lett. 36, L08102.

Farrugia, C.J., Freeman, M.P., Burlaga, L.F., Lepping, R.P., Takahashi, K., 1993. The Earth's magnetosphere under continued forcing: substorm activity during the passage of an interplanetary magnetic cloud. J. Geophys. Res. 98, 7657–7671.

Farrugia, C.J., Berdichevsky, D.B., 2004. Evolutionary signatures in complex ejecta and their driven shocks. Ann. Geophys. 22, 3679–3698.

Farrugia, C.J., Jordanova, V.K., Thomsen, M.F., Lu, G., Cowley, S.W.H., Ogilvie, K.W., 2006. A two-ejecta event associated with a two-step geomagnetic storm. J. Geophys. Res. 111, A11104, doi:101029/2006JA011893..

Feldman, W.C., Asbridge, J.R., Bame, S.J., Montgomery, M.D., Gary, S.P., 1975. Solar wind electrons. J. Geophys. Res. 80, 4181–4196.

Galvin, A.B., Kistler, L.M., Popecki, M.A., Farrugia, C.J., et al., 2008. The plasma and suprathermal ion composition (PLASTIC) investigation on the STEREO observatories. Space Sci. Rev. 136 (1–4), 437–486.

Goldstein, H., 1983. On the field configuration in magnetic clouds. In: Solar Wind Five. NASA Conf. Publ., CP-2280, 731.
Gosling, J.T., Baker, D.N., Bame, S.J., Feldman, W.C., Zwickl, R.D., Smith, E.J., 1987. Bidirectional solar wind electron heat flux events. J. Geophys. Res. 92, 8519–8535.
Gosling, J.T., Birn, J., Hesse, M., 1995. Three-dimensional magnetic reconnection and the magnetic topology of coronal mass ejection events. Geophys. Res. Lett. 22 (8), 869–872.
Gosling, J.T., Riley, P., McComas, D.J., Pizzo, V.J., 1998. overexpanding coronal mass ejections at high heliographic latitudes: observations and simulations. J. Geophys. Res. 103 (A2), 1941–1954.
Gosling, J.T., Pizzo, V.J., 1999. Formation and evolution of corotating interaction regions and their three dimensional structure. In: Balogh, A., Gosling, J.T., Jokipii, J.R., Kallenbach, R., Kunov, H. (Eds.), Corotating Interaction Regions Space Sciences Series of ISSI. Kluwer, Norwell, USA, pp. 21–52.
Gosling, J.T., Skoug, R.M., Feldman, W.C., McComas, D.J., 2002. Symmetric suprathermal electron depletions on closed field lines in the solar wind. Geophys. Res. Lett. 29 (12), 1573, doi:10.1029/2001GL013949.
Hau, L.N., Sonnerup, B.U.Ö., 1999. Two-dimensional coherent structures in the magnetopause: recovery of static equilibria from single-spacecraft data. J. Geophys. Res. 104 (A4), 6899–6917.
Howard, R.A., et al., 2008. Sun Earth connection coronal and heliospheric investigation (SECCHI). Space Sci. Rev. 136 (1–4), 67–115.
Hu, Q., Sonnerup, B.U.Ö., 2002. Reconstruction of magnetic clouds in the solar wind. J. Geophys. Res. 107 (A7), 1142, doi:10.1029/2001JA000293.
Hu, Q., Smith, C.W., Ness, N.F., Skoug, R.M., 2003. Double flux-rope magnetic cloud in the solar wind at 1 AU. Geophys. Res. Lett. 30 (7), 1385, doi:10.1029/2002GL016653.
Jian, L., Russell, C.T., Luhmann, J.G., Skoug, R.M., 2006. Properties of stream interactions at 1 AU during 1995–2004. Solar Phys. 239, 337–392, doi:10.0007/s11207-006-0132-3.
Kamide, Y., Yokoyama, N., Gonzalez, W., Tsurutani, B.T., Daglis, I.A., Brekke, A., Masuda, S., 1998. Two-step development of geomagnetic storms. J. Geophys. Res. 103, 6917–6921.
Kilpua, E.K.J., Luhmann, J.G., Gosling, J., Li, Y., Elliott, H., Russell, C.T., Jian, L., Galvin, A.B., Larson, D., Schroeder, P., Simunac, K., Petrie, G., 2009. Small solar wind transients and their connection to the large-scale coronal structure. Solar Phys. 256, 327–344.
Klein, L.W., Burlaga, L.F., 1982. Interplanetary magnetic clouds at 1 AU. J. Geophys. Res. 87, 613–624.
Lavraud, B., Borovsky, J.E., 2008. Altered solar wind-magnetosphere interaction at low Mach numbers: coronal mass ejections. J. Geophys. Res. 113, A00B08, doi:10.1029/2008JA013192.
Leitner, M., Farrugia, C.J., Möstl, C., Ogilvie, K.W., Galvin, A.B., Schwenn, R., Biernat, H.K., 2007. Consequences of the force-free model of magnetic clouds for their heliospheric evolution. J. Geophys. Res. 112, A06113, doi:10.1029/2006JA011940.
Lepping, R.P., Jones, J.A., Burlaga, L.F., 1990. Magnetic field structure of interplanetary magnetic clouds at 1 AU. J. Geophys. Res. 95 (A8), 11957–11965.
Lepping, R.P., et al., 1995. The wind magnetic field investigation. Space Sci. Rev. 71, 207–229.
Lepping, R.P., Berdichevsky, D.B., Burlaga, L.F., et al., 2001. The Bastille day magnetic clouds and upstream shocks: near-Earth interplanetary observations. Solar Phys. 204, 287–305.
Lin, R.P., et al., 1995. A three-dimensional plasma and energetic particle investigation for the wind spacecraft. Space Sci. Rev. 71, 125–153.
Lopez, R.E., 1987. Solar cycle invariance in solar wind proton temperature relationships. J. Geophys. Res. 92, 11189–11194.
Luhmann, J.G., Curtis, D.W., Schroeder, P., et al., 2008. STEREO IMPACT investigation goals measurements, and data products. Space Sci. Rev. 136 (1–4), 117–184.
Lundquist, S., 1950. Magnetohydrostatic fields. Ark. Fys. 2, 361.
Marubashi, K., 1986. Structure of the interplanetary magnetic clouds and their origins. Adv. Space Res. 6 (6), 335–338.
Möstl, C., Miklenic, C., Farrugia, C.J., Veronig, A., Temmer, M., Galvin, A., Vrsnak, B., Biernat, H.K., 2008. Two-spacecraft reconstruction of a magnetic cloud and comparison to its solar source. Ann. Geophys. 26, 3139–3152.
Möstl, C., Farrugia, C.J., Temmer, M., Miklenic, C., Veronig, A.M., Galvin, A.B., Leitner, M., Biernat, H.K., 2009a. Linking remote imagery of a coronal mass ejection to its in situ signatures at 1 AU. Astrophys. J. Lett. 705, L180–L185.
Möstl, C., Farrugia, C.J., Miklenic, C., Temmer, M., Galvin, A.B., Luhmann, J.G., Kilpua, E.K.J., Leitner, M., Nieves-Chincilla, T., Veronig, A., Biernat, H.K., 2009b. Multi-spacecraft recovery of a magnetic cloud and its origin from magnetic reconnection on the Sun. J. Geophys. Res. 114, A04102, doi:10.1029/2008JA013657.
Möstl, C., Farrugia, C.J., Leitner, M., Kilpua, E.K.J., Biernat, H.K., Galvin, A.B., Luhmann, J.G., 2009c. Optimized reconstruction of a small magnetic cloud using STEREO-WIND observations. Solar Phys. 256, 427–441, doi:10.1007/s11207-009-9360-7.
Montgomery, M.D., Bame, S.J., Hundhausen, A.J., 1968. Solar wind electrons: vela 4 measurements. J. Geophys. Res. 73, 4999–5003.
Morley, S.K., Rouillard, A.P., Freeman, M.P., 2009. Recurrent substorm activity during the passage of a corotating interaction region. J. Atmos. Solar Terr. Phys. 71, 1073–1081.
Neugebauer, M., Goldstein, R., 1997. Particle and field signatures of coronal mass ejections in the solar wind. In: Crooker, N.U., Joselyn, J.A., Feynman, J. (Eds.), Coronal Mass Ejections, Geophysical Monograph Series, vol. 99. AGU, Washington, DC, pp. 245–251.
Ogilvie, K.W., Scudder, J.D., Sugiura, M., 1971. Electron energy flux in the solar wind. J. Geophys. Res. 76, 8165–8173.
Ogilvie, K.W., et al., 1995. SWE A comprehensive plasma instrument for the wind spacecraft. Space Sci. Rev. 71, 55–77.
Pilipp, W.G., Miggenrieder, H., Montgomery, M.D., Mühlhäuser, K.-H., Rosenbauer, H., Schwenn, R., 1987. Unusual electron distribution functions in the solar wind derived from the Helios plasma experiment: double-strahl distributions and distributions with an extremely anisotropic core. J. Geophys. Res. 92 (A2), 1093–1101.
Qiu, J., Hu, Q., Hpward, T.A., Yurchyshyn, V.B., 2007. On the magnetic flux budget in low-corona magnetic reconnection and interplanetary coronal mass ejections. Astrophys. J. 659, 758–772.
Rouillard, A.P., et al., 2008. First imaging of corotating interaction regions using the STEREO spacecraft. Geophys. Res. Lett. 35, L10110, doi:10.1029/2008GL033767.
Rouillard, A.P., Savani, N.P., Davies, J.A., Lavraud, B., Forsyth, R.J., Morley, S.K., Opitz, A., Sheeley, N.R., Burlaga, L.F., et al., 2009. A multispacecraft analysis of a small-scale transient entrained by solar wind streams. Solar Phys. 256 (1–2), 307–326.
Rouillard, A.P., Davies, J.A., Lavraud, B., Forsyth, R.J., Savani, N.P., et al., 2010a. Intermittent release of transients in the slow solar wind: I, remote sensing observations. J. Geophys. Res. 115, A04103, doi:10.1029/2009JA014471.
Rouillard, A.P., Lavraud, B., Davies, J.A., Savani, N.P., Burlaga, L.F., Forsyth, R.J., Sauvaud, J.-A., et al., 2010b. Intermittent release of transients in the slow solar wind: 2. In situ evidence. J. Geophys. Res. 115, A04104, doi:10.1029/2009JA014472.
Rouillard, A.P., Lavraud, B., Sheeley, N.R., Davies, J.A., Burlaga, L.F., Savani, N.P., Jacquey, C., Forsyth, R.J., 2010c. White-light and in-situ comparison of a forming merged interaction region. Astrophys. J. 719, 1385, doi:10.1088/0004-637X/719/1385.
Sauvaud, J.-A., Larson, D., Aoustin, C., et al., 2008. The IMPACT solar electron analyzer SWEA. Space Sci. Rev. 136 (1–4), 227–239.
Sheeley, N., Wang, Y.-M., Hawley, S.H., Brueckner, G.E., et al., 1997. Measurements of flow speeds in the corona between 2 and 30 Rs. Astrophys. J. 484, 472–478.
Sheeley, N.R., Walters, J.H., Wang, Y.M., Howard, R.A., 1999. Continuous tracking of coronal outflows: two kinds of coronal mass ejections. J. Geophys. Res. 104, 24739–24768 doi:10.1029/1999JA900308.
Sheeley, N.R., et al., 2008. Heliospheric images of the solar wind at Earth. Astrophys. J. 675, 853–862.
Shodhan, S., Crooker, N., Kahler, S., Fitzenreiter, R., Larson, D., Lepping, R., Siscoe, G., Gosling, J., 2000. Counterstreaming electrons in magnetic clouds. J. Geophys. Res. 105 (A12), 27261–27268.
Sonnerup, B.U.Ö, Cahill, L.J., 1967. Magnetopause structure and attitude from Explorer 12 observations. J. Geophys. Res. 72, 171–183.
Tsurutani, B.T., Gonzalez, W.D., 1987. The cause of high intensity long-duration continuous AE activity (HILDCAAs): interplanetary Alfvén waves trains. Planet. Space Sci. 35, 405–412.
Vourlidas, A., Howard, R.A., 2006. The proper treatment of coronal mass ejection brightness: a new methodology and implications for observations. Astrophys. J. 642, 1216–1221.
Wang, Y.-M., Sheeley Jr., N.R., Socker, D.G., Howard, R.A., Rich, N.B., 2000. The dynamical nature of coronal streamers. J. Geophys. Res. 105, 25133–25142.
Yamamoto, T.T., Kataoka, R., Inoue, S., 2010. Helical lengths of magnetic clouds from the magnetic flux conservation. Astrophys. J. 710, 456–461.